Publisher: NPG; Journal: Nature: Nature; Article Type: Physics article
MS nr: 2019-07-11046

Compression of curium pyrrolidinedithiocarbamate enhances covalency

Joseph M. Sperling[1], Evan J. Warzecha[1], Cristian Celis-Barros[1], Dumitru-Claudiu Sergentu[2], Xiaoyu Wang[2], Bonnie E. Klamm[1], Cory J. Windorff[1], Alyssa N. Gaiser[1], Frankie D. White[1], Drake A. Beery[1], Alexander T. Chemey[1], Megan A. Whitefoot[1], Brian N. Long[1], Kenneth Hanson[1], Paul Kögerler[3], Manfred Speldrich[3]†, Eva Zurek[2]†, Jochen Autschbach[2]† & Thomas E. Albrecht-Schmitt[1]†

[1]Department of Chemistry and Biochemistry, Florida State University, Tallahassee, FL, USA.

[2]Department of Chemistry, University at Buffalo, State University of New York, Buffalo, NY, USA.

[3]Institut für Anorganische Chemie, RWTH Aachen University, Aachen, Germany

†e-mail: manfred.speldrich@rwth-aachen.de; ezurek@buffalo.edu; jochena@buffalo.edu; talbrechtschmitt@fsu.edu

Curium is unique in the actinide series because its half-filled $5f^7$ shell has a lower energy than other $5f^n$ configurations, rendering it both redox-inactive and resistant to forming chemical bonds that engage the 5*f* shell[1–3]. This is even more pronounced in gadolinium, curium's lanthanide analogue, owing to the contraction of the 4*f* orbitals with respect to the 5*f* orbitals[4]. However, at high pressures metallic curium undergoes a transition from localized to itinerant 5*f* electrons[5]. This transition is accompanied by a crystal structure dictated by the magnetic interactions between curium atoms[5,6]. Therefore, the question arises of whether the frontier metal orbitals in curium(III)–ligand interactions can also be modified by applying pressure, and thus be induced to form metal–ligand bonds with a degree of covalency. Here we report experimental and computational evidence for changes in the relative roles of the 5*f*/6*d* orbitals in curium–sulfur bonds in $[Cm(pydtc)_4]^-$ (pydtc, pyrrolidinedithiocarbamate) at high pressures (up to 11 gigapascal). We compare these results to the spectra of $[Nd(pydtc)_4]^-$ and of a Cm(III) mellitate that possesses only curium–oxygen bonds. Compared with the changes observed in the $[Cm(pydtc)_4]^-$ spectra, we observe smaller changes in the *f–f* transitions in the $[Nd(pydtc)_4]^-$ absorption spectrum and in the *f–f* emission spectrum of the Cm(III) mellitate upon pressurization, which are related to the smaller perturbation of the nature of their bonds. These results reveal that the metal orbital contributions to the curium–sulfur bonds are considerably enhanced at high pressures and that the 5*f* orbital involvement doubles between 0 and 11 gigapascal. Our work implies that covalency in actinides is complex even when dealing with the same

ion, but it could guide the selection of ligands to study the effect of pressure on actinide compounds.

Synthesis and structure determination

The reaction of $^{248}Cm(NO_3)_3 \cdot nH_2O$ with excess $[NH_4][pydtc]$ in methanol results in the formation of the ammonium salt of tetrakis(pydtc)Cm^{3+}, $[NH_4][Cm(pydtc)_4] \cdot 2CH_3OH$ (**Cm-1**), in approximately 80% yield in the form of very pale yellow, block-shaped single crystals within 15 min. Structural analysis of these crystals shows that they contain Cm^{3+} cations bound by four bidentate $pydtc^-$ ligands creating an eight-coordinate geometry, as shown in Fig. 1. This polyhedron is best approximated by a trigonal dodecahedron with D_{2d} symmetry. The Cm–S bond lengths range from 2.8655(14) Å to 2.9116(13) Å with an average of 2.8841(14) Å (where parentheses indicate standard errors) and compare well with those reported recently for $Cm(dtc)_3(phen)$ (dtc, *N*,*N*-diethyldithiocarbamate; phen, phenanthroline)[7].

Temperature- and pressure-dependent spectroscopy

The absorption spectrum from a single crystal of **Cm-1** shows characteristic sharp *f*–*f* transitions consistent with Cm^{3+} (Extended Data Fig. 1)[8–10]. More importantly, photoluminescence spectra acquired as a function of temperature show an unusually large splitting of 743 cm^{-1} of the primary peak centred at 16,635 cm^{-1} (611 nm), as depicted in Fig. 2a. This value appears to be exceeded only by Cm^{3+} doped into ThO_2 (ref. [11]). This transition arises from the four different energy levels of the emissive Group A state, which is composed primarily from an admixture of the $^6D_{7/2}$, $^6P_{7/2}$ states[10–13]. The weighted average excited-state lifetime of this state is 92 μs. For comparison, a Cm^{3+} mellitate ($[C_6(CO_2)_6]^{6-}$) compound, $Cm_2(mellitate)(H_2O)_8 \cdot 2H_2O$ (**Cm-2**), was prepared and then characterized using the same methods. This compound contains only Cm–O bonds to either the carboxylate moieties of the ligand or water molecules. Here the four ligand-field levels of the emissive state cannot be resolved from the main peak centred at 16,750 cm^{-1} (597 nm) even at low temperatures (Extended Data Fig. 2).

The photoluminescence behaviour of **Cm-1** under pressure and at low temperatures is shown in Fig. 2. The phosphorescence response of **Cm-2** is shown in Extended Data Fig. 2. Temperature-induced shifts of the photoluminescence wavelengths are not observed in either complex. However, there is a steady increase in the phosphorescence intensity in both complexes as the temperature is lowered to 93 K. The increasing intensity is due to the decreased

probability of vibrational relaxation at lower temperatures. The large spike in intensity coincides with the freezing of the oil in which the crystals are submerged.

The pressure response is different for **Cm-1** and **Cm-2**. **Cm-1** shows a substantial bathochromic shift as pressure is applied, with maximum wavelength (λ_{max}) increasing linearly by approximately 2 nm GPa^{-1}, from 611.38 ± 0.03 nm at ambient pressure (1 atm, 10^{-4} GPa) to 633.4 ± 0.01 nm at 10.65 GPa (Fig. 3). Additionally, the feature broadens markedly with increasing pressure. At low pressures, the full-width at half-maximum (FWHM) of the feature increases from 337 ± 2 cm^{-1} to 1,098 ± 5 cm^{-1} and the ligand-field splitting is no longer discernible. This contrasts with the behaviour of **Cm-2**, which is affected to a much lesser extent by increasing the pressure. The photoluminescence λ_{max} of **Cm-2** shifts by only about 8 nm from 0 to 7 GPa, from 597.34 ± 0.07 nm at ambient pressure to 605.43 ± 0.05 nm, and this shift is not accompanied by sizable broadening—although a higher-energy shoulder does begin to appear at higher pressures. The peak shifts and intensity changes of both curium complexes with respect to pressure are shown in Fig. 3.

The changes in the absorbance spectra of both **Cm-1** and **Cm-2** with respect to pressure also show considerable differences. Whereas the *f*–*f* transitions of **Cm-1** are quickly obscured by the broadband transition belonging to the $pydtc^-$ ligand, they show sizable bathochromic shifts before they are obscured, with peak shifts between 180 cm^{-1} and 245 cm^{-1} at 4 GPa. Comparatively, the absorption features of **Cm-2** remain unobscured and show only small bathochromic shifts of less than 130 cm^{-1} up to 7 GPa. These shifts are much closer to that observed for the Nd^{3+} analogue of the pydtc complex (**Nd-1**), which shows a shift of approximately 100 cm^{-1} over 8 GPa. The absorption responses to pressure for **Cm-1**, **Nd-1** and **Cm-2** are shown in Extended Data Fig. 1. Single crystals of all three compounds fracture into microcrystals that diffract too weakly for high-pressure structure refinements. However, bulk polycrystalline samples of **Nd-1** were crushed with effective pressures of up to 2 GPa and did not show amorphization, decomposition or secondary phase formation, as determined by powder X-ray diffraction measurements[14]. Macroscopic samples of **Cm-1** cannot be crushed for safety reasons, but the expectation is that the crystallites will exhibit a similar response to **Nd-1**.

Theoretical understanding of pressure-induced changes in bonding

To understand the origins of the effects of pressure on **Cm-1** and **Cm-2**, the structures of the crystals were optimized from 0 to 11 GPa (up to 7 GPa for **Cm-2**) using density functional theory (DFT)[15]. The experimental and optimized ambient-pressure unit cell parameters agree well (Extended Data Table 1), as do the Cm–S and Cm–O bond lengths (with root-mean-square deviations of 0.022 Å and 0.026 Å, respectively). The electronic structures were determined using the multiconfigurational complete active space self-consistent field (CASSCF) method and multiconfigurational pair-density functional theory (MC-pDFT), including spin-orbit coupling when indicated (see Methods section 'Computational details'). The Cm^{3+} free ion has a $5f^7 6d^0$ electronic ground state that is an admixture of ~80% ^8S and ~13% ^6P terms owing to the strong spin–orbit coupling[9,16–19], which is reproduced in our calculations. In the low-energy electronic spectrum of Cm^{3+} in host crystals, emission occurs at ~17,000 cm^{-1} and ~20,000 cm^{-1} from a $J = 7/2$ and a $J = 5/2$ level, respectively, with the largest contributors being the ^6D and ^6P ion terms[9,17,18]. Using MC-pDFT+SO, we find that the lowest excited $J = 7/2$ multiplet of Cm^{3+} is a $^6D_{7/2}$ level and the calculated energy is in reasonable agreement with the experimental data (Extended Data Table 2). Using CASSCF plus dynamic correlation via second-order perturbation theory (PT2+SO), the first excited level is a $^6P_{7/2}$ and the calculated energy is too high compared to the experimental value (Extended Data Table 2). The calculation of the electronic structure of Cm^{3+} is challenging because only a limited amount of dynamic electron correlation is captured with PT2 and a practical active space[16]. Thus, the results from MC-pDFT+SO were used further.

The bathochromic shifts (ΔE) observed experimentally for **Cm-1** and **Cm-2** under pressure are reproduced well by the MC-pDFT+SO calculations (see Extended Data Table 2), irrespective of the applied functional approximation. Compared to the shift observed for **Cm-2** between 0 and 7 GPa, the larger bathochromic shift of the emissive $^6D_{7/2}$ band of **Cm-1** between 11 GPa and 0 GPa stems from a pressure-induced enhancement of the ligand field and from changes in the metal–ligand bonding that manifests in the $^8S_{7/2}$ ground state as well as in the $^6D_{7/2}$ emitting state. In the ^8S ground state of **Cm-1**, the Cm 5*f* canonical orbitals split in energy by 812 cm^{-1} at 0 GPa and by 1,449 cm^{-1} at 11 GPa, clearly demonstrating the enhanced ligand field.

These spectroscopic changes are accompanied by a shrinkage of the average distance between Cm^{3+} and the coordinating ligand sulfur atoms, which ranges from 2.8655(14) Å to

2.9916(13) Å at 0 GPa to the calculated values of 2.662 Å to 2.866 Å at 11 GPa. These results in an average bond decrease by approximately 0.139 Å with a maximum change of 0.2179 Å. The dihedral angles between opposing ligands for the 0-GPa structure are 4° and 9°, whereas at 11 GPa they twist to 13° and 67°. For comparison, the average distance between Cm^{3+} and the coordinating mellitate/water oxygen atoms in **Cm-2** is 2.478 Å and 2.421 Å at 0 and 7 GPa, respectively; that is, an average bond decrease of only 0.057 Å.

The analysis of the natural localized molecular orbitals (NLMOs) of MC-pDFT+SO (Extended Data Fig. 3) and CASSCF scalar relativistic (SR) (Fig. 4, Extended Data Table 3) wavefunctions for the ground state confirms the enhanced pressure-induced metal–ligand bonding in **Cm-1** compared to **Cm-2**. Both methods qualitatively support that covalency increases at high pressures, albeit with differences in the polarization of the bonds and 5*f*-electron involvement. With MC-pDFT+SO, the effect of the 6*d* and 5*f* orbitals on the Cm–S bonds of **Cm-1** increases slightly with pressure. This is a consequence of the pressure-induced shrinkage of the coordinating ligand sphere around the Cm^{3+} centre, which favours better orbital overlap (hybridization) and hence ligand-to-metal bonding. CASSCF-SR calculations (using the ORCA package; Fig. 4) show a 5*f* subshell that is more involved in covalency and sensitive to the pressure applied, with variations of up to 12% when comparing the 0-GPa to the 11-GPa complexes. The enhanced bonding as a function of pressure can be quantified using Wiberg bond orders, delocalization indices and effective bond orders, which all show the same trend. These values are listed in Extended Data Table 4 (see also Extended Data Fig. 3).

Based on the above experimental data and theory, we can conclude that the greater radial extension of 5*f* orbitals compared to 4*f* orbitals is not the sole factor dictating these pressure-induced changes in bonding. The nature of the ligands also affects the overlap of the *f* orbital with the ligand orbital, in addition to the extension of the metal orbital. In **Cm-1**, the increased polarizability of the $pydtc^-$ ligands compared to mellitate clearly plays an important role in its pressure response. These observations could provide guidance for the selection of actinide systems to study at high pressures.

Online content Any methods, additional references, Nature Research reporting summaries, source data, extended data, supplementary information, acknowledgements, peer review information; details of author contributions and competing interests; and statements of data and code availability are available at [DOI link].

Received 23 July 2019; accepted 21 April 2020.

1. Wybourne, B. G. *Spectroscopic Properties of Rare Earths* (Wiley, 1965).

2. Silver, M. A. et al. Electronic structure and properties of berkelium iodates. *J. Am. Chem. Soc.* **139**, 13361–13375 (2017).

3. Bagus, P. S., Ilton, E. S., Martin, R. L., Jensen, H. J. A. & Knecht, S. Spin–orbit coupling in actinide cations. *Chem. Phys. Lett.* **546**, 58–62 (2012).

4. Edelstein, N. M., Klenze, R., Fanghänel, T. & Hubert, S. Optical properties of Cm(III) in crystals and solutions and their application to Cm(III) speciation. *Coord. Chem. Rev.* **250**, 948–973 (2006).

5. Heathman, S. et al. A high-pressure structure in curium linked to magnetism. *Science* **309**, 110–113 (2005).

6. Moore, K. et al. Emergence of strong exchange interaction in the actinide series: the driving force for magnetic stabilization of curium. *Phys. Rev. Lett.* **98**, 236402 (2007).

7. Cary, S. K. et al. A series of dithiocarbamates for americium, curium, and californium. *Dalton Trans.* **47**, 14452–14461 (2018).

8. Carnall, W. T. & Fields, P. A study of the complexes of curium (III) by absorption spectrometry. *J. Am. Chem. Soc.* **81**, 4445–4449 (1959).

9. Carnall, W. T. & Wybourne, B. G. Electronic energy levels of the lighter actinides: U^{3+}, Np^{3+}, Pu^{3+}, Am^{3+}, and Cm^{3+}. *J. Chem. Phys.* **40**, 3428–3433 (1964).

10. Carnall, W. T. & Rajnak, K. Electronic energy level and intensity correlations in the spectra of the trivalent actinide aquo ions. II. Cm^{3+}. *J. Chem. Phys.* **63**, 3510–3514 (1975).

11. Kolbe, W., Edelstein, N. M., Finch, C. & Abraham, M. Zero-field splittings of Gd^{3+} and Cm^{3+} in CeO_2 and ThO_2. *J. Chem. Phys.* **58**, 820–821 (1973).

12. Kim, J., Klenze, R. & Wimmer, H. Fluorescence spectroscopy of curium(III) and application. *Eur. J. Solid State Inorg. Chem.* **28**, 347–356 (1991).

13. Yusov, A. Luminescence of transplutonium elements in solutions and its application. *Radiokhimiya* **35**, 1–14 (1993).

14. Dachille, F. & Roy, R. High-pressure phase transformations in laboratory mechanical mixers and mortars. *Nature* **186**, 34–71 (1960).

15. Perdew, J. P. et al. Restoring the density-gradient expansion for exchange in solids and surfaces. *Phys. Rev. Lett.* **100**, 136406 (2008).

16. Jung, J., Atanasov, M. & Neese, F. Ab initio ligand-field theory analysis and covalency trends in actinide and lanthanide free ions and octahedral complexes. *Inorg. Chem.* **56**, 8802–8816 (2017).

17. Murdoch, K., Nguyen, A., Edelstein, N., Hubert, S. & Ga, J. Two-photon absorption spectroscopy of Cm^{3+} in $LuPO_4$. *Phys. Rev. B* **56**, 3038–3045 (1997).

18. Illemassene, M., Murdoch, K., Edelstein, N. & Krupa, J. Optical spectroscopy and crystal field analysis of Cm^{3+} in $LaCl_3$. *J. Lumin.* **75**, 77–87 (1997).

19. Sytsma, J., Murdoch, K., Edelstein, N. M., Boatner, L. & Abraham, M. Spectroscopic studies and crystal-field analysis of Cm^{3+} and Gd^{3+} in $LuPO_4$. *Phys. Rev. B* **52**, 12668 (1995).

Fig. 1 | Molecular structure of Cm-1. a, Thermal ellipsoid plot of the $[Cm(pydtc)_4]^-$ anion in **Cm-1**, with the Cm^{3+} cation complexed by four bidentate $pydtc^-$ ligands, plotted at 50% probability. **b**, Structure of the **Cm-1** anion, showing the ligand environment.

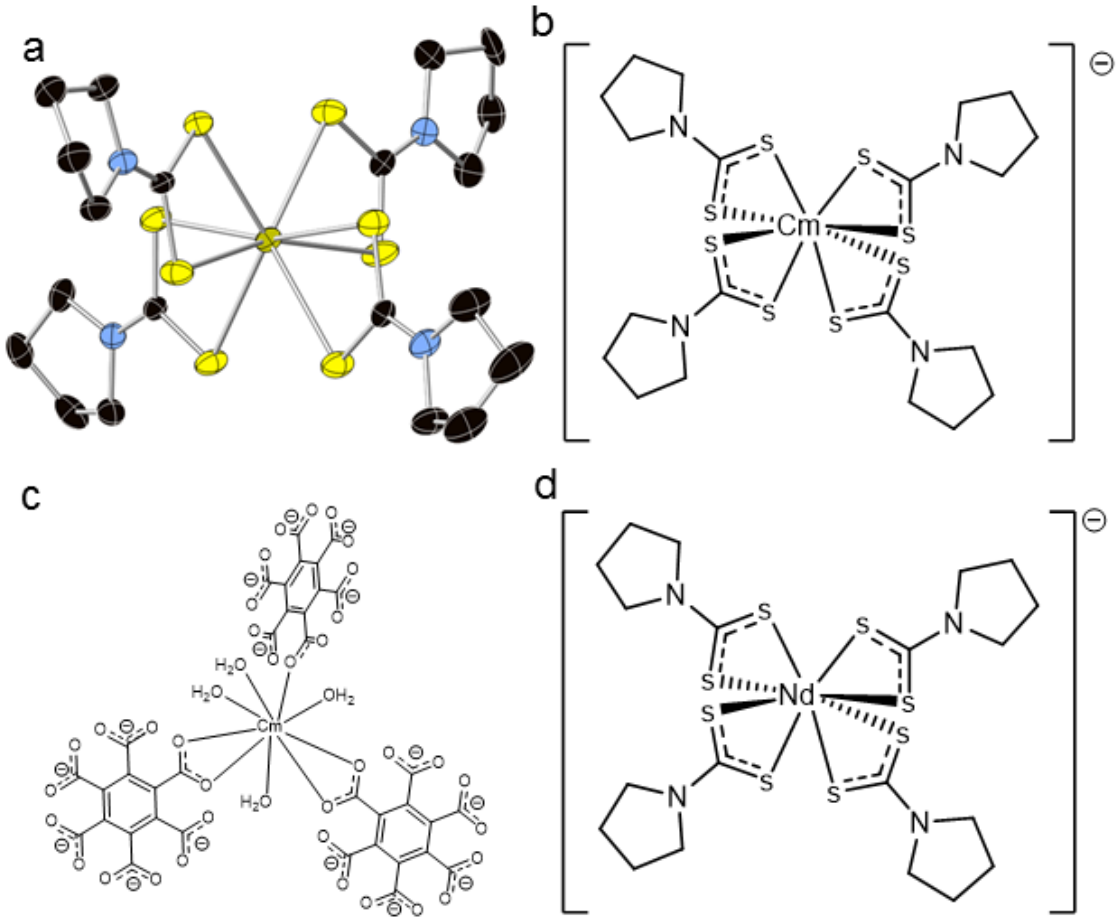

Fig. 2 | Phosphorescence spectra of $[NH_4][Cm(pydtc)_4]\cdot 2CH_3OH$ (Cm-1). **a**, Temperature-dependent spectra of **Cm-1** showing the large splitting of the Stark levels of the emissive state. **b**, Pressure-dependent spectra of **Cm-1** showing how the sharp features broaden upon the application of pressure. The excitation wavelength, λ_{ex} = 420 nm for both spectra.

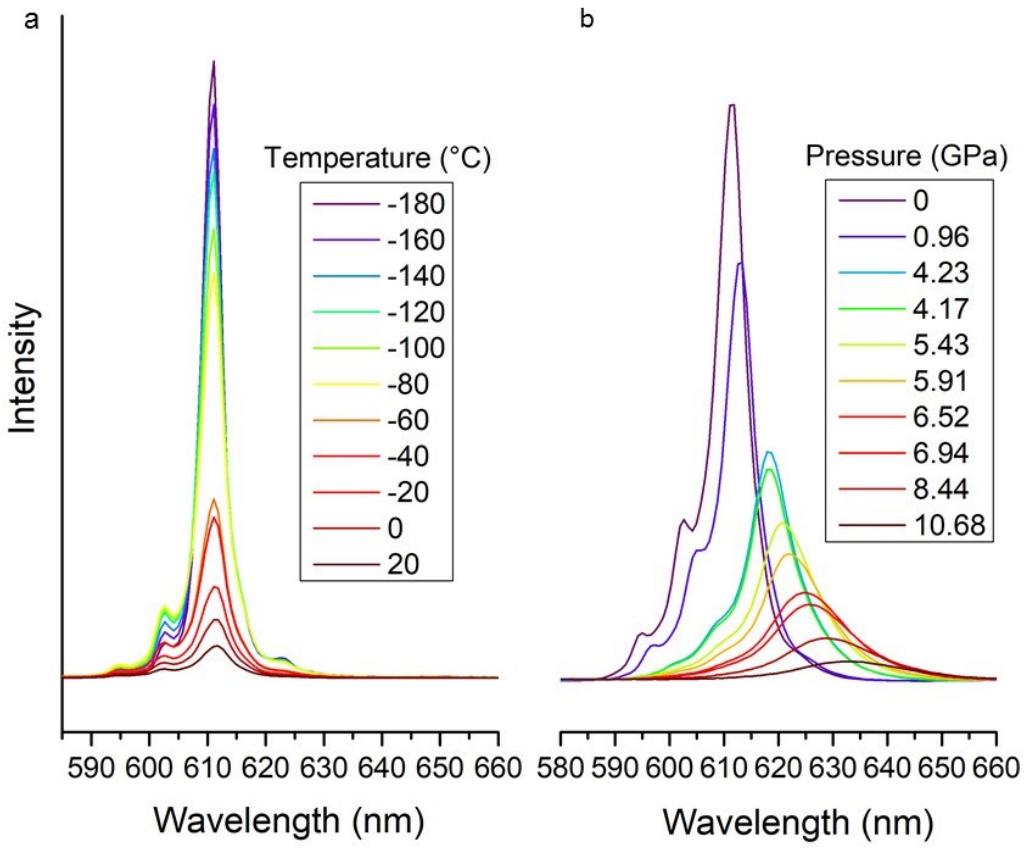

Fig. 3 | Comparison of pressure response of Cm-1 and Cm-2. a–**d**, Emission intensity (**a**) and λ_{max} (**b**) of **Cm-1**, and emission intensity (**c**) and λ_{max} (**d**) of **Cm-2**. The steady decrease in intensity as well as the steady increase in wavelength for **Cm-1** demonstrates smooth changes upon pressurization, whereas **Cm-2** does not show a consistent change in its intensity plot. The peak position of **Cm-2** does increase as pressure is applied; however, it increases at a much slower rate and without the linear trend observed for **Cm-1**. Error bars represent the standard error in the pressure calculation.

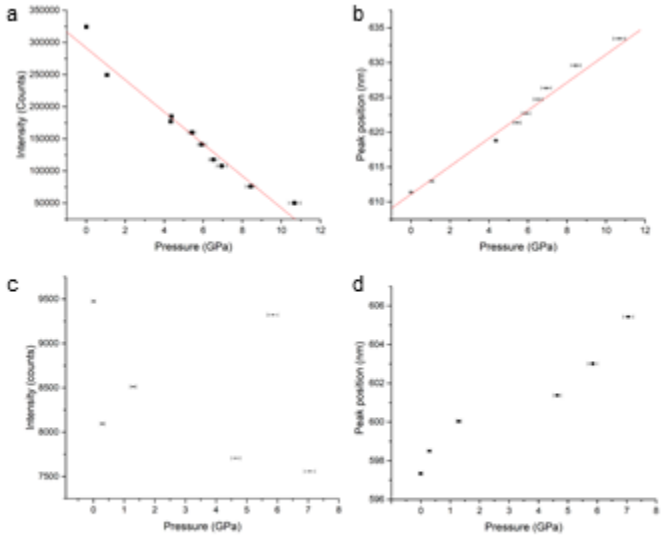

Fig. 4 | Selected NLMO describing the Cm–S bond in Cm-1. Example showing the greatest change in the Cm–S bond composition by the application of pressure. Comparing the selected NLMO at 0 and 11 GPa shows that the main difference is the increased Cm contribution at the higher pressure, as well as the 5*f* involvement. Further NLMO compositions can be found in Extended Data Fig. 3.

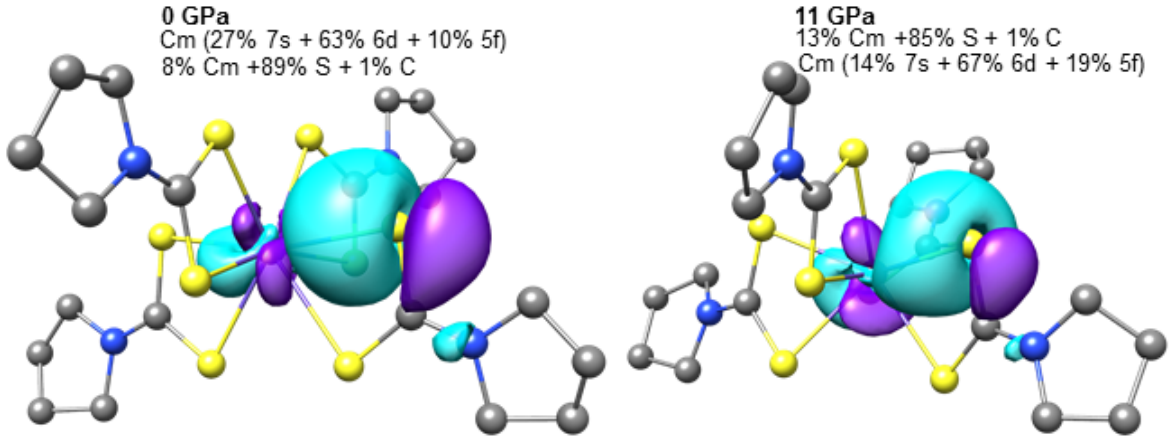

METHODS

General considerations

Caution: ^{248}Cm (half-life $t_{1/2}$ = 348,000 y; specific activity 4.14 mCi g^{-1}) represents a serious health risk owing to α emission (5.078 MeV, 75%) to daughter ^{244}Pu ($t_{1/2}$ = 80,800,000 y; specific activity 18.1 μCi g^{-1}) and a nearly 8% spontaneous fission rate creating a large flux of neutrons of up to 80 mrem h^{-1} (1 rem = 0.01 Sv) for the sample used. All manipulations of the material were performed in a Category II nuclear hazard facility equipped with an air-handling system containing a series of eight filters, including carbon and HEPA filters. HCl, HNO_3, MeOH, EtOH, $(NH_4)_2CO_3$, ammonium pyrollidinedithiocarbamate, $[NH_4]$[pydtc] and mellitic acid (H_6mell) were all purchased from Sigma-Aldrich and used without further purification. Ultrapure water was distilled before use and was used for diluting acids.

Syntheses

$[NH_4][Cm(pydtc)_4]\cdot 2CH_3OH$ (Cm-1)

4 mg (0.016 mmol) of $^{248}Cm^{3+}$ dissolved in 2 M HCl was dried to a soft residue roughly formulated as $^{248}CmCl_3\cdot nH_2O$. The residue was then dissolved in 2 ml of UltraPure water (18.2 MΩ cm) and was precipitated with $(NH_4)_2CO_3$ to form $^{248}Cm_2(CO_3)_3$, which was centrifuged to a pellet and washed with ultrapure water three times. The precipitate was further treated with 200 μl of concentrated HNO_3. The 200-μl solution was transferred to a 7-ml scintillation vial and dried to a residue formulated as $^{248}Cm(NO_3)_3\cdot nH_2O$. The residue was dissolved in 0.5 ml of methanol and was then charged with excess $[NH_4]$[pydtc] dissolved in 0.5 ml of methanol. A light-yellow powder precipitated immediately, as shown in Extended Data Fig. 4. Then, 1 ml of methanol was added and the powder was left to settle. The mother liquor was then transferred into a new 7-ml vial under a gentle stream of nitrogen to cool and concentrate the methanolic solution, yielding light-yellow crystals within 10 min.

$^{248}Cm_2$mellitate$(H_2O)_8\cdot 2H_2O$ (Cm-2)

The synthesis of **Cm-2** was inspired by another publication[20]. A pellet of $^{248}Cm_2(CO_3)_3$ containing 3 mg (0.012 mmol) of ^{248}Cm was dissolved in a minimum amount of 12 M HCl and was dried to a soft residue. The hydrated $^{248}CmCl_3$ residue was dissolved in 500 μl of ultrapure

water and was transferred to a 6-ml shell vial inside a 20-ml scintillation vial. A 500-µl solution of mellitic acid in fourfold excess dissolved in water was added to the ^{248}Cm, and the aqueous ^{248}Cm solution was layered with ethanol. Ethanol was then added to the 20-ml vial for both vapour and layer diffusion. Small block-like crystals formed overnight, as shown in Extended Data Fig. 4.

$[NH_4][Nd(pydtc)_4]\cdot 2CH_3OH$ (Nd-1)

12 mg (0.027 mmol) of $Nd(NO_3)_3\cdot 6H_2O$ was dissolved in 0.25 ml of MeOH in a 6-ml scintillation vial. The Nd solution was then charged with excess $[NH_4][pydtc]$ dissolved in 0.5 ml of MeOH. Single crystals suitable for X-ray diffraction measurements grew within 1 min in ~90% yield.

Crystallographic studies

Crystals were isolated directly from their respective mother liquors and submerged into Krytox oil. They were mounted on 75-µm MiTeGen mounts and optically aligned using a digital camera attached to a Bruker D8 Quest X-ray diffractometer. Single-crystal X-ray diffraction data were obtained using Mo Kα radiation (0.71073 Å) from an IµS X-ray source at 150 K using an Oxford Cyrostream N-Helix. A collection strategy was generated by using the Bruker APEXIII software. Unit cell determinations were completed using the Bruker software as well. The structure was solved using direct methods refined on F^2 (F= Structure factor) by full-matrix least squares with SHELXTL software using the OLEX2 GUI[21,22]. Cm scattering factors were not available in the software at the time of solving the structures and were manually added to the instruction file[23]. Two disordered methanol molecules in **Cm-1** and **Nd-1** were accounted for using SQUEEZE[24].

Ultraviolet–visible–near-infrared spectroscopy

A CRAIC Technologies microspectrophotometer was used to collect absorbance and photoluminescence data in the ultraviolet–visible–near-infrared (UV-Vis-NIR) region using a mercury light source for absorption and a xenon lamp for luminescence from single crystals. Integration times for the UV-Vis and NIR detectors were produced automatically for the absorption data and manually for the photoluminescence data using the CRAIC software. Selected crystals were transferred onto a separate slide and placed on a Linkam temperature-

control stage. The photoluminescence data were acquired in increments of 20 K from 93 K to 293 K.

Pressure application

Stainless steel gaskets were indented from 200 μm to 60–65 μm. A 150-μm-diameter hole was drilled in the indent and loaded onto a Diacell TozerDAC-Xray diamond anvil cell. Single crystals of the compounds were loaded into the cell with a ruby sphere as a pressure standard and petroleum jelly as a pressure-transmitting medium. The pressure was determined using the ruby fluorescence method[25]. Peaks were fitted with Lorentz curves.

Steady-state and time-resolved emission

Data were collected at room temperature using an Edinburgh FLS980 spectrometer. The samples were excited using the light output from a housed 450-W Xe lamp passed through a single-grating (1,800 lines per millimetre, 250 nm blaze) Czerny–Turner monochromator and finally a 1-nm-bandwidth slit. Emission from the sample was first passed through the appropriate long-pass colour filter, then a single-grating (1,800 lines per millimetre, 500 nm blaze) Czerny–Turner monochromator (1 nm bandwidth) and finally detected by a Peltier-cooled Hamamatsu R928 photomultiplier tube.

The dynamics of the emission decay were monitored using the spectrometer's multi-channel scaling acquisition mode with 405.2-nm excitation from a 60-W microsecond flashlamp (pulse width <2.5 μs) at a repetition rate of 100 Hz with data collection for 5,000 counts. Time-resolved emission data were fitted using the Edinburgh software package and using the bi-exponential (**Cm-1**) and single exponential function (**Cm-2**) shown in equation (1). A weighted average of the lifetime (τ) was calculated using equation (2).

$$y = A_1 e^{-k_1 x} + A_2 e^{-k_2 x} + y_0 \quad (1)$$

$$\tau_i = 1/k_i, \quad \langle \tau \rangle = \sum \left(A_i \tau_i^2 \right) / \sum \left(A_i \tau \right) \quad (2)$$

Where y is intensity (counts), A_i are pre-exponential factors, k_i are decay constants, and y_0 is an offset.

Computational details

Periodic structure calculations

Crystal structure optimizations were performed using DFT with the PBEsol exchange-correlation functional[15], as implemented in the Vienna ab initio simulation package[26]. The atomic valence shells (5*f*, 6*s*, 6*d*, 6*p* and 7*s* for Cm; 1*s* for H; 2*s* and 2*p* for C, O and N; 3*s* and 3*p* for S) were represented by a plane-wave basis set with an energy cutoff of 520 eV, with the core shells treated using the projector augmented-wave method[27]. Because of the large unit cell size, only the Gamma point was considered. The calculations assumed a ferromagnetic configuration with seven unpaired electrons on each Cm^{3+}. The crystal structures were optimized from 0 to 12 GPa (**Cm-1**) or 7 GPa (**Cm-2**) with an increment of 1 GPa, yielding the cell parameters shown in Extended Data Table 1.

Molecular electronic structure calculations

The structures of the **Cm-1** and **Cm-2** complexes were excised from the crystal structures optimized from 0 to 11 GPa and 7 GPa, respectively. First, the metal–ligand bonding in **Cm-1** and **Cm-2** was investigated with DFT using the Amsterdam DFT package (ADF, 2017 release). Owing to the large size of a **Cm-2** unit (a Cm centre, three mellitate ligands and four water molecules), molecular DFT (as well as CASSCF+SO and MC-pDFT+SO) calculations were conducted on a (truncated) **Cm-2′** model structure (Extended Data Fig. 5). **Cm-2′** retains the Cm coordination of a **Cm-2** unit while substituting the mellitate $-C_6(CO_2)_4$ terminals by optimized $-CF_3$ terminals. We note that $-CF_3$ was chosen owing to its similarity to the $-CO_2$ unit regarding electron-attractive properties. The $-CF_3$ units were optimized with DFT using the generalized gradient functional PBE (Perdew-Burke-Ernzerhof) , all-electron triple-ζ doubly polarized TZ2P basis sets for all atoms, and a large frozen-core setting. For both **Cm-1** and **Cm-2′**, the ground-state (^8S) electron densities, which were used subsequently for NLMO bonding analyses, were converged with PBE as well as with the B3LYP and PBE0 hybrid functionals, TZ2P basis sets for all atoms, and no frozen-core setting. All DFT calculations used the SR all-electron zeroth-order regular-approximation Hamiltonian. NLMO analyses were carried out with the NBO6 program. The Cm^{3+} free ion and the **Cm-1** and **Cm-2′** complexes were subjected to ab initio wavefunction calculations, performed with OpenMolcas[28], to obtain insight into the variation of the electronic structure and metal–ligand bonding. SR multiconfigurational CASSCF)[29]

calculations used the $5f^7$ Cm^{3+} orbitals and electrons for the active space. All possible spin states were calculated, that is, 1 octet, 48 sextets, 392 quartets and 784 doublets. The SR second-order Douglas–Kroll–Hess (DKH2) Hamiltonian was used, along with all-electron ANO-RCC basis sets contracted to polarized triple-ζ quality for the Cm, S and O centres, and polarized double-ζ quality for N, C, F and H. Spin–orbit coupling (SOC) was treated via state interaction and the AMFI formalism, in a basis of selected complete active space (CAS) SR states and diagonal energies (either CASSCF or with dynamic correlation effects included). Dynamic correlation was treated by multireference state-specific CAS PT2 and MC-pDFT[30], the latter using the tPBE and tLSDA on-top functionals. In the PT2 calculations for **Cm-1**, the correlation orbital space was defined with the 'afreeze' setting of OpenMolcas; that is, the occupied orbitals that share at least 0.1 of their density with the S and the Cm centres were retained along with all the virtual orbitals. Metal–ligand bonding was assigned with NLMO analyses of the MC-pDFT+SO wavefunctions attained with the NBO6 program[31] and a new OpenMolcas interface[32].

Molecular electronic structure calculations were also performed using the ORCA 4.1.0 package[33] on the structures at 0 and 11 GPa for further treatment of the wavefunction using the quantum theory of atoms in molecules (QTAIM) with the AIMAll software[34]. The basis sets used were the all-electron SARC-TZVP for Cm and def2-TZVP for C, S and H. As in the OpenMolcas calculations, the DKH2 Hamiltonian was used to account for SR effects. CAS-SR(7,7) wavefunctions were used to obtain QTAIM metrics. The NBO6 program[31] linked to ORCA was used to obtain the corresponding NLMOs.

An alternative way to understand covalency is provided by the differences in the potential $V_{BCP}(r)$ and kinetic $G_{BCP}(r)$ energy densities at the bond critical point (BCP) that are a function of the position, **r**, since they are descriptors derived from the electron density $\rho(r)$. If the total energy density $H_{BCP}(r)$ is negative, the potential energy densities predominate, and therefore the concentration of $\rho(r)$ at the BCP is favoured. This is in line with the Lewis concept of covalency as electrons shared between two atoms. It is well known that covalency in actinides is partial or polarized. In terms of QTAIM, this implies that $1 < |V(r)|/G(r) < 2$ is purely ionic for $|V(r)|/G(r) < 1$ and formally covalent for $|V(r)|/G(r) > 2$ (ref. [35]). Thus, the degree of polarization can be obtained through the percentage by which $V_{BCP}(r)$ predominates over $G_{BCP}(r)$. Our results indicate that the concentration of $\rho_{BCP}(r)$ not only increases, but also stabilizes by up to 68% for some of the Cm–S bonds in the structure at 11 GPa with respect to the 0-GPa structure.

Moreover, the polarization of the bond is reduced as the pressure is increased, implying that covalent interactions are increasing (from 14% up to 23%), as shown in Extended Data Table 3.

Additional insight is obtained through analysis of the QTAIM topology of the electron density (see section 'Computational details'). Within QTAIM, information about actinide covalency[36] is obtained by examining the electron density at a BCP, $\rho_{BCP}(r)$, and the delocalization indices $\delta_{BCP}(r)$, which enable an evaluation of the bond order. Therefore, any increase in the orbital overlap will be echoed by an increase in $\rho_{BCP}(r)$ and $\delta_{BCP}(r)$; whereas for degeneracy-driven covalency, only $\delta_{BCP}(r)$ will show a considerable increase[37,38]. Extended Data Table 3 show sizable increases in both $\rho_{BCP}(r)$ and $\delta_{BCP}(r)$ with increasing pressure from 0 to 11 GPa, consistent with increased metal–ligand overlap and increased covalency. Other covalency measures from the QTAIM framework corroborate the increased covalency under pressure and show a decreased bond polarization and energetic stabilization of some of the Cm–S bonds when pressurizing from 0 to 11 GPa. Therefore, regardless of the method used to address covalency in the 0-GPa and 11-GPa **Cm-1** complexes, the conclusion is qualitatively the same: covalency increases through heightened orbital overlap of both the Cm^{3+} 6*d* orbitals and the 5*f* subshells.

CONDON 3.0 calculations

The magnetic susceptibility characteristics of **Cm-1** were also derived using the collected spectroscopic data. Simulation of these data from the emission spectra (Fig. 2) of the lowest $^6D_{7/2}$ state to the ground state $^8S_{7/2}$ allows us to calculate the magnetic susceptibility of **Cm-1** as a function of pressure. The data were fitted to a 'full-model' Hamiltonian implemented in the computational framework CONDON 3.0[39], where the relevant spin–orbit coupling and Slater–Condon parameter were chosen on the basis of the optical spectra of Cm^{3+}:ThO_2 and used as constants[11].

Initial sets of most ligand-field parameters (B_q^k ; Wybourne notation[22]) were again adopted from spectroscopically determined energy levels for Cm^{3+}:$LuPO_4$ with D_{2d} symmetry so that we require only one additional ligand-field parameter B_0^2 and there is no fixed relationship between B_4^4/B_0^4 and B_4^6/B_0^6 . These results are in excellent agreement with the experimental emission spectra (Quality of the fit = 1×10^{-3}%) of the lowest $^6D_{7/2}$ state to the ground state $^8S_{7/2}$,

yielding a ligand field characterized by $B_0^2 = 478\ \mathrm{cm}^{-1}$, $B_0^4 = 3,090\ \mathrm{cm}^{-1}$, $B_4^4 = 1,750\ \mathrm{cm}^{-1}$, $B_0^6 = -1,924\ \mathrm{cm}^{-1}$ and $B_4^6 = 790\ \mathrm{cm}^{-1}$ for 0 GPa and $B_0^2 = 635\ \mathrm{cm}^{-1}$, $B_0^4 = 3,456\ \mathrm{cm}^{-1}$, $B_4^4 = 1,546\ \mathrm{cm}^{-1}$, $B_0^6 = -5,100\ \mathrm{cm}^{-1}$ and $B_4^6 = 954\ \mathrm{cm}^{-1}$ for 8 GPa, which is also in line with point-charge electrostatic model calculations. Moreover, the composition of the ground term ($^8S_{7/2}$, 78%; $^5D_{7/2}$, 19%) is consistent with the spectroscopic data of Cm^{3+}:$LuPO_4$.

The absorbance response to pressure for **Cm-1** corresponds to substantial differences in the magnetic behaviour of the splitting of the ground state $^8S_{7/2}$, which increases dramatically under pressure, and a stronger temperature dependence of the magnetic moment (μ_{eff}) is expected. The overall ligand-field splitting of the $^8S_{7/2}$ ground state into m_J substates amounts to 17.7 cm^{-1} for 0 GPa to 27.5 cm^{-1} for 8 GPa. However, the ground term for Cm^{3+} is only 78% $^8S_{7/2}$ because spin–orbit coupling mixes in substantial amounts of the $^6D_{7/2}$ (18%) and $^6P_{7/2}$ (2%) states, as well as higher terms, resulting in a reduced μ_{eff} value of $7.66\mu_B$ at room temperature (μ_B, Bohr magneton). For the $4f^7$ analogue, Gd(III), crystal-field splitting of the ground $J = 7/2$ term is indeed of the order of about 0.2 cm^{-1}, with a corresponding g value (dimensionless magnetic moment) of 1.9993 ($\mu_{eff} = 7.91\mu_B$ at room temperature; grey line in Extended Data Fig. 6); this example shows a substantial difference between f^7 actinide and lanthanide systems. In addition to the pressure dependence, we observe a stronger temperature dependence of the magnetic moment by changing the single-ion effects under pressure; such behaviour is not observed in $4f^7$ systems.

Data availability

Crystallographic information files have been deposited in the Cambridge Crystallographic Data Centre (CCDC https://www.ccdc.cam.ac.uk/structures/) with deposition numbers 1927752 (**Cm-1**), 1927751 (**Cm-2**) and 1930252 (**Nd-1**).

20. da Luz, L. L. et al. Inkjet printing of lanthanide-organic frameworks for anti-counterfeiting applications. *ACS Appl. Mater. Interfaces* **7**, 27115–27123 (2015).

21. Sheldrick, G. SHELXT – integrated space-group and crystal-structure determination. *Acta Crystallogr. A* **71**, 3–8 (2015).

22. Dolomanov, O. V., Bourhis, L. J., Gildea, R. J., Howard, J. A. K. & Puschmann, H. OLEX2: a complete structure solution, refinement and analysis program. *J. Appl. Cryst.* **42**, 339–341 (2009).

23. Milburn, G. International tables for X-ray crystallography. *Acta Crystallogr. B* **32**, 2732 (1983).

24. Spek, A. L. PLATON SQUEEZE: a tool for the calculation of the disordered solvent contribution to the calculated structure factors. *Acta Crystallogr. C* **71**, 9–18 (2015).

25. Chijioke, A. D., Nellis, W., Soldatov, A. & Silvera, I. F. The ruby pressure standard to 150 GPa. *J. Appl. Phys.* **98**, 114905 (2005).

26. Kresse, G. & Hafner, J. Ab initio molecular dynamics for liquid metals. *Phys. Rev. B* **47**, 558 (1993).

27. Blöchl, P. E. Projector augmented-wave method. *Phys. Rev. B* **50**, 17953 (1994).

28. Aquilante, F. et al. Molcas 8: new capabilities for multiconfigurational quantum chemical calculations across the periodic table. *J. Comput. Chem.* **37**, 506–541 (2016).

29. Roos, B. O., Taylor, P. R. & Si, P. E. A complete active space SCF method (CASSCF) using a density matrix formulated super-CI approach. *Chem. Phys.* **48**, 157–173 (1980).

30. Gagliardi, L. et al. Multiconfiguration pair-density functional theory: a new way to treat strongly correlated systems. *Acc. Chem. Res.* **50**, 66–73 (2017).

31. Glendening, E. D., Landis, C. R. & Weinhold, F. NBO 6.0: natural bond orbital analysis program. *J. Comput. Chem.* **34**, 1429–1437 (2013).

32. Sergentu, D.-C., Duignan, T. J. & Autschbach, J. Ab initio study of covalency in the ground versus core-excited states and X-ray absorption spectra of actinide complexes. *J. Chem. Phys. Lett.* **9**, 5583–5591 (2018).

33. Neese, F. Software update: the ORCA program system, version 4.0. *Wiley Interdiscip. Rev. Comput. Mol. Sci.* **8**, e1327 (2018).

34. Keith, T. AIMA11 (TK Gristmill Software, 2017).

35. Espinosa, E., Alkorta, I., Elguero, J. & Molins, E. From weak to strong interactions: a comprehensive analysis of the topological and energetic properties of the electron density distribution involving X−H ··· F−Y systems. *J. Chem. Phys.* **117**, 5529–5542 (2002).

36. Neidig, M. L., Clarck, D. L. & Martin, R. L. Covalency in *f*-element complexes. *Coord. Chem. Rev.* **257**, 394–406 (2013).

37. Kerridge, A. Quantification of *f*-element covalency through analysis of the electron density: insights from simulation. *Chem. Commun.* **53**, 6685–6695 (2017).

38. Lu, E. et al. Emergence of the structure-directing role of *f*-orbital overlap-driven covalency. *Nat. Commun.* **10**, 634 (2019).

39. Speldrich, M., van Leusen, J. & Kögerler, P. CONDON 3.0: an updated software package for magnetochemical analysis-all the way to polynuclear actinide complexes. *J. Comput. Chem.* **39**, 2133–2145 (2018).

Acknowledgements All experimental studies and the high-pressure molecular geometry and electronic structure calculations were supported by the US Department of Energy, Office of Science, Office of Basic Energy Sciences, Heavy Elements Chemistry Program under award numbers DE-FG02-13ER16414 (TEAS) and DE-SC0001136 (J.A.). Theoretical studies after high-pressure evaluation were supported by the US Department of Energy through the Center for Actinide Science and Technology (CAST) funded by the Energy Frontiers Research Program under award number DE-SC0016568. We are grateful for the assistance and supervision of the Office of Environmental Health and Safety at Florida State University, specifically J. A. Johnson and A. L. Gray of the Office of Radiation Safety for their facilitation of these studies. D.-C.S., X.W., E.Z. and J.A. thank the Center for Computational Research (CCR) at the University at Buffalo for providing computational resources. E.Z. acknowledges the NSF (DMR-1827815) for financial support.

Author contributions J.M.S., E.J.W., B.E.K., C.J.W., A.N.G., F.D.W., A.T.C., M.A.W., B.N.L., D.A.B., K.H. and T.E.A.-S. conceived, designed and carried out the synthetic, spectroscopic, crystallographic and high-pressure experiments. P.K., M.S., D.-C.S., C.C.-B., X.W., E.Z. and J.A. carried out the quantum mechanical calculations. All authors discussed and co-wrote the manuscript.

Competing interests The authors declare no competing interests.

Additional information

Supplementary information is available for this paper at [DOI link].

Correspondence and requests for materials should be addressed to M.S., J.A., E.Z. or T.E.A.-S.

Peer review information *Nature* thanks Olle Eriksson, Stephen Moggach and Tonya Vitova for their contribution to the peer review of this work.

Extended Data Fig. 1 | Absorbance spectra as a function of pressure. a, *f–f* transitions in **Cm-1** spectra show large bathochromic shifts as pressure is applied; however, the $pydtc^-$ ligand-based broadband absorption quickly obscures the Cm^{3+} transitions. **b**, In **Cm-2**, these transitions are not competing with any broadband ligand-based transitions; however, the *f–f* transitions show much smaller shifts up to high pressures than those observed for **Cm-1**. **c**, The shifts observed in **Nd-1**, the Nd^{3+} analogue of **Cm-1**, are more similar to those of **Cm-2** than those of **Cm-1**.

Extended Data Fig. 2 | Photoluminescence data for Cm-1 and Cm-2. a, **b**, Phosphorescence spectra of **Cm-2** as a function of temperature (**a**) and pressure (**b**) (λ_{ex} = 420 nm). **c**, **d**, Emission decay curves (λ_{ex} = 443 nm, λ_{em} = 609 nm) for **Cm-1** (**c**) and **Cm-2** (**d**) (λ_{ex} = 434 nm, λ_{em} = 596 nm). Even at low temperatures the Stark levels are not clearly resolved in **Cm-2**. Pressure does not induce considerable broadening, and only minor bathochromic shifts are observed. **Cm-1** has a weighted lifetime of 92 μs and **Cm-2** has a lifetime of 18 μs. The longer lifetime of **Cm-1** compared to **Cm-2** is reflected in the increased intensity of the emission.

Extended Data Fig. 3 | Depiction of two-centre two-electron *σ*(Cm–S) NLMOs. **a**, NLMOs (isosurface of ±0.02) obtained from the MC-pDFT+SO/tPBE wavefunctions of the $^8S_{7/2}$ ground state and the photoluminescent $^6D_{7/2}$ state of **Cm-1** at 0 GPa (left) and 11 GPa (right). NLMO compositions (averaged over the eight Cm–S bonds), aggregate Cm Wiberg bond index (WBI) and NLMO/NPA (natural population analysis)-based effective bond order ($EBO^{NLMO/NPA}$, obtained from the NLMO shared occupancies and bonding–antibonding overlap). **b**, NLMOs, aggregate Cm WBI, and $EBO^{NLMO/NPA}$ of the $^8S_{7/2}$ ground state of **Cm-2** (theoretical model) .

Extended Data Fig. 4 | Reaction and crystal images. a, **b**, The reaction of Cm^{3+} before (**a**) and after (**b**) the addition of $[NH_4][pydtc]$. **c**, Single crystal upon excitation with 420-nm light at 20 °C (bottom), −80 °C (middle) and −180 °C (top). **d**, **e**, **Cm-1** crystals before (**d**) and during (**e**) excitation with 420-nm light. **f**, **g**, Single crystals before (**f**) and during (**g**) irradiation with 420-nm light. **h**, The reaction vial of **Cm-2**. **Cm-2** crystal under 420-nm light at 20 °C (left), −80 °C (middle) and −180 °C (right).

Extended Data Fig. 5 | Computational models and actual structure of Cm-2. Geometry of **Cm-2** units (nine-coordinated Cm by three mellitate ligands and four water ligands) at 0 GPa (left, wire frame) and 7 GPa (right, wire frame) superimposed with model geometry **Cm-2′** ('balls & sticks'). The model geometries retain the original Cm coordination while substituting the mellitate $C_6(CO_2)_4$ terminals by CF_3. The model geometries were used for MC-pDFT+SO calculations and DFT ground-state bonding analyses.

Extended Data Fig. 6 | Temperature dependence of μ_{eff} of Cm-1. Two different pressures are shown, 0 GPa (red line) and 8.0 GPa (blue line). Inset, total ligand-field splitting of the $^8S_{7/2}$ term (left; red, 0 GPa; blue 8 GPa) and total splitting of the first excited $^6D_{7/2}$ term (right; red, 0 GPa; blue, 8 GPa; black, calculated energies).

Extended Data Table 1 | Unit cell parameters optimized for Cm-1 and Cm-2 at different pressures

Extended Data Table 2 | Experimental and calculated relative energy (in units of cm^{-1}) between the J = 7/2 ($^8S_{7/2}$) ground state and the J = 7/2 ($^6D_{7/2}$ for MC-pDFT+SO and $^6P_{7/2}$ for CAS+SO) excited state of Cm-1 and Cm-2 at different applied pressures

[a]The CAS+SO calculation coupled 1o, 48s, 392q and 784d LS (Russell-Saunders) spin states and the MC-pDFT+SO calculation coupled 1o, 48s and 119q LS spin states. o, s, q and d stand for spin-octet, sextet, quartet and doublet, respectively.
[b]Emission energy shift (ΔE) from 0 to 11 Gpa or 7 GPa. The calculated shifts listed in parentheses were extracted from the emission band maxima.
[c]tPBE functional.
[d]tLSDA functional.

Extended Data Table 3 | Bonding σ-type NLMOs involving Cm(III) in $[Cm(pydtc)_4]^-$ (Cm-1) at 0 and 11 GPa from the CAS-SR wavefunction

NLMOs correspond to those with the largest contribution to the bond.
*Localized molecular orbital bond orders, which distinguish bonding from antibonding contributions.

Extended Data Table 4 | QTAIM parameters at the bond critical point derived from CAS-SR wavefunctions

Electron density ρ(r) in units of e $Å^{-3}$ (e, electron charge). $V(r)$, $G(r)$ and $H(r)$ correspond to the potential, kinetic and total energy densities, respectively (in in kJ mol^{-1} $Å^{-3}$). The delocalization indices $\delta(r)$ are compared to Wiberg bond orders (WBO).